ACSNANO

www.acsnano.org

ARTICLE

Proton-Dominated Reversible Aqueous Zinc Batteries with an Ultraflat Long Discharge Plateau

Yuanhe Sun,[⊥] Zhaofeng Lian,[⊥] Zhiguo Ren, Zeying Yao, Yaru Yin, Ping Huai, Fangyuan Zhu, Yaobo Huang, Wen Wen, Xiaolong Li,* Renzhong Tai,* and Daming Zhu*

Cite This: *ACS Nano* 2021, 15, 14766−14775

Read Online

ACCESS | Metrics & More | Article Recommendations | Supporting Information

ABSTRACT: **Aqueous zinc batteries (AZBs) are considered promising candidates for large-scale energy storage systems because of their low cost and high safety. However, currently developed AZB cathodes always suffer from the intense charge repulsion of multivalent-ion and complex multiphase electrochemistry, resulting in an insufficient cycling life and impracticable high-sloping discharge profile. Herein, we found that the synthesized ultrathin Bi_2O_2Se nanosheets can effectively activate stable protons storage in AZBs rather than large zinc ions. This proton-dominated cathode provides an ultraflat discharge plateau (72% capacity proportion) and exhibits long-term cyclability as 90.64% capacity retention after 2300 cycles at 1 A g^{-1}. Further *in situ* synchrotron X-ray diffraction, *ex situ* X-ray photoelectronic spectroscopy, and density functional theory confirm the energy storage mechanism regarding the highly reversible proton insertion/extraction process. Benefiting from the proton-dominated fast dynamics, reliable energy supply (>81.5% discharge plateau capacity proportion) is demonstrated at a high rate of up to 10 A g^{-1} and in the frozen electrolyte below −15 °C. This work provides a potential design of high-performance electrode materials for AZBs.**

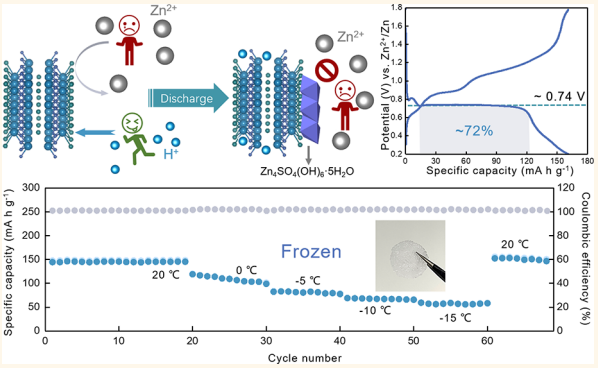

KEYWORDS: *aqueous zinc battery, Bi_2O_2Se nanosheets, proton domination, in situ synchrotron X-ray diffraction, ultraflat discharge plateau*

Aqueous zinc batteries (AZBs) are attracting intensive attention as a possible substitute for lithium batteries (LBs) due to the high theoretical capacity (820 mA h g^{-1}), suitable redox potential (−0.76 V vs standard hydrogen electrode), and low cost (USD $2 kg^{-1}) of zinc metal.[1−3] Considering that aqueous electrolytes (approximately 1 S cm^{-1}) have much higher ionic conductivities than nonaqueous electrolytes (approximately 1−10 mS cm^{-1}) and the natural safety and abundance of aqueous solutions, AZBs have higher potential as grid-scale electrochemical energy storage application than other beyond-lithium-ion batteries.[4,5] Various cathode materials for AZBs have been developed to meet the requirements of high energy density and long cycling stability, such as manganese-based oxides,[6] Prussian blue analogues,[7] and zinc orthovanadates.[8] Additionally, Ni et al. recently proposed employing $Na_3V_2(PO_4)_2O_{1.6}F_{1.4}$ as cathodes in zinc batteries[9] with a discharge capacity of 155 mA h g^{-1} at 50 mA g^{-1}, and Ti_2CT_x MXenes[10] were also used and showed a reversible capacity of 138 mA h g^{-1} at 100 mA g^{-1}. However, due to the large size of zinc ions (~0.74 Å) and the high zinc-ion intercalation energy barrier stemming from strong electrostatic repulsion by host lattice, the proposed cathodes usually exhibit inferior cycling stability, greatly limiting their practical operation.[11,12]

Recently, the hybrid ions storage has been investigated in zinc-based energy storage devices.[13,14] For instance, the reversible zinc-ion/proton co-insertion into layered host cathodes, such as manganese dioxide,[15] sodium vanadate,[16] and potassium vanadate,[17] was demonstrated in mild AZB systems. The auxiliary insertion of protons diminishes the strong Coulombic ion−lattice interactions and further enhances the ion insertion kinetics. Unfortunately, with the

Received: May 31, 2021
Accepted: August 24, 2021
Published: August 25, 2021

Downloaded via XINJIANG UNIV on September 30, 2021 at 07:55:21 (UTC).
See https://pubs.acs.org/sharingguidelines for options on how to legitimately share published articles.

© 2021 American Chemical Society

https://doi.org/10.1021/acsnano.1c04636
ACS Nano 2021, 15, 14766−14775

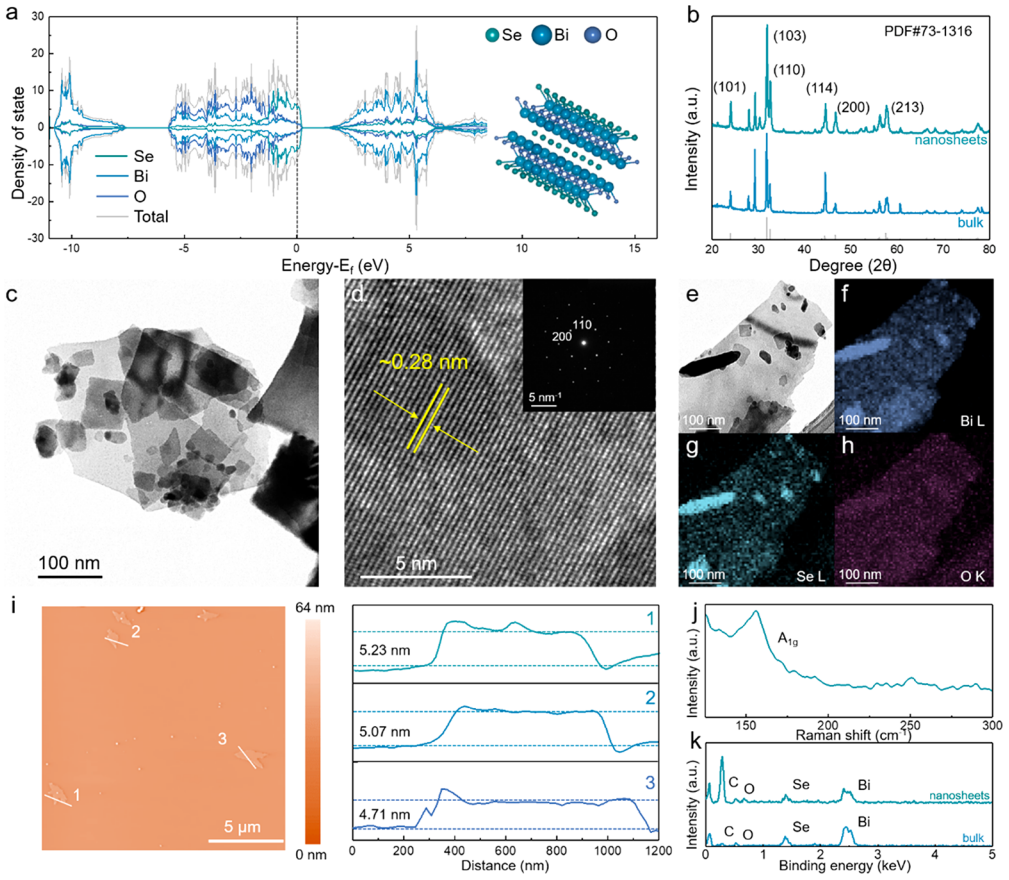

Figure 1. (a) PDOS of the four-layer Bi_2O_2Se nanosheets. Upper and lower panels represent the spin-up and spin-down states, respectively. The Fermi level is set to zero and indicated by the gray dashed line as an eye guide. The inset illustration shows the structure of Bi_2O_2Se. (b) XRD patterns of the bulk Bi_2O_2Se and BOSNs. (c) TEM images and (d) the corresponding HRTEM images with the SAED pattern. (e) TEM images and the corresponding (f) Bi, (g) Se, and (h) O elemental mapping images of BOSNs. (i) AFM images of the BOSNs washed with deionized water. (j) Raman spectra of the BOSNs. (k) EDS spectra of the BOSNs and bulk Bi_2O_2Se.

insertion of a high proportion of zinc ions, the host lattices gradually collapse during the charge/discharge processes, which leads to significant capacity fading. A feasible strategy is to increase the proportion of protons in charge carriers. Compared with zinc ions, protons possess a significantly smaller charge radius,[18] a weaker Coulomb barrier, and extremely fast diffusion ability in electrolytes/electrodes with Grotthuss conduction,[19] which may enable extraordinarily low-temperature performance[20] and superior capacity delivery over a satisfactory electrode life span.[21] To capitalize on these features, Zhao et al. presented a Ni-doped MnO_2 cathode that greatly boosted the proton intercalation capability of AZB,[22] and Zhang et al. reported a water-proton co-intercalation MoO_3 cathode blocking Zn-ion intercalation pathways while allowing proton intercalation/diffusion.[23] As expected, these specially designed cathodes do deliver an enhanced stable capacity based on proton storage along with high electrode structural stability. In general, owing to the small charge radius and fast kinetics of proton, the proton-dominated intercalation electrochemistry is believed to preserve integrated two-phase reactions in the cathode, with stable Gibson formation energy of the products and reactants of the reaction.[24] Nevertheless, the discharge profiles reported previously suggest the uncontrollable evolution of potentials and complex sloping regions, and the non-Nernst-type curves depicted in the proton-dominated intercalation cathodes should be attributed to the solid-solution mechanism and intermediate phase formation extensively involved. Thus, by exploration of a suitable cathode solely based on proton-dominated intercalation chemistry to endow assembled AZBs with high cycling stability, a flat discharge plateau and low-temperature performance is highly desired but remains at a nascent stage.

As a low cost and nontoxicity stratified compound,[25] bismuth-based chalcogenides such as Bi_2Se_3 have been investigated as AZBs cathode with zinc-ion/proton co-intercalation mechanism,[26] which possess the potential to realize the proton-dominated electrochemical process. In the meantime, the synergistic combination of O^{2-} and Se^{2-} may improve affinity for protons and electrode stability in weak acid electrolyte. Herein, we demonstrate a proton-dominated AZBs with ultrathin Bi_2O_2Se nanosheets (BOSNs) as cathode materials, and the prepared BOSN//Zn battery demonstrates a long stable discharge plateau with a typical capacity of 162 mA h g^{-1} at 0.1 A g^{-1}. *In situ* synchrotron X-ray diffraction (SXRD), *ex situ* X-ray photoelectron spectroscopy (XPS), and density functional theory (DFT) calculations confirm the suggested insertion/extraction process of proton. Benefiting from proton-dominated insertion/extraction process, an enhanced cycling performance of 2300 cycles at 1 A g^{-1} with 90.64% capacity retention is also achieved at a Coulombic efficiency of nearly 100%. More importantly, the proton-dominated electrochemical process promotes the low-temperature performance of the batteries; therefore, the proposed cell can provide a capacity of 84 mA h g^{-1} under icing conditions

https://doi.org/10.1021/acsnano.1c04636
ACS Nano 2021, 15, 14766−14775

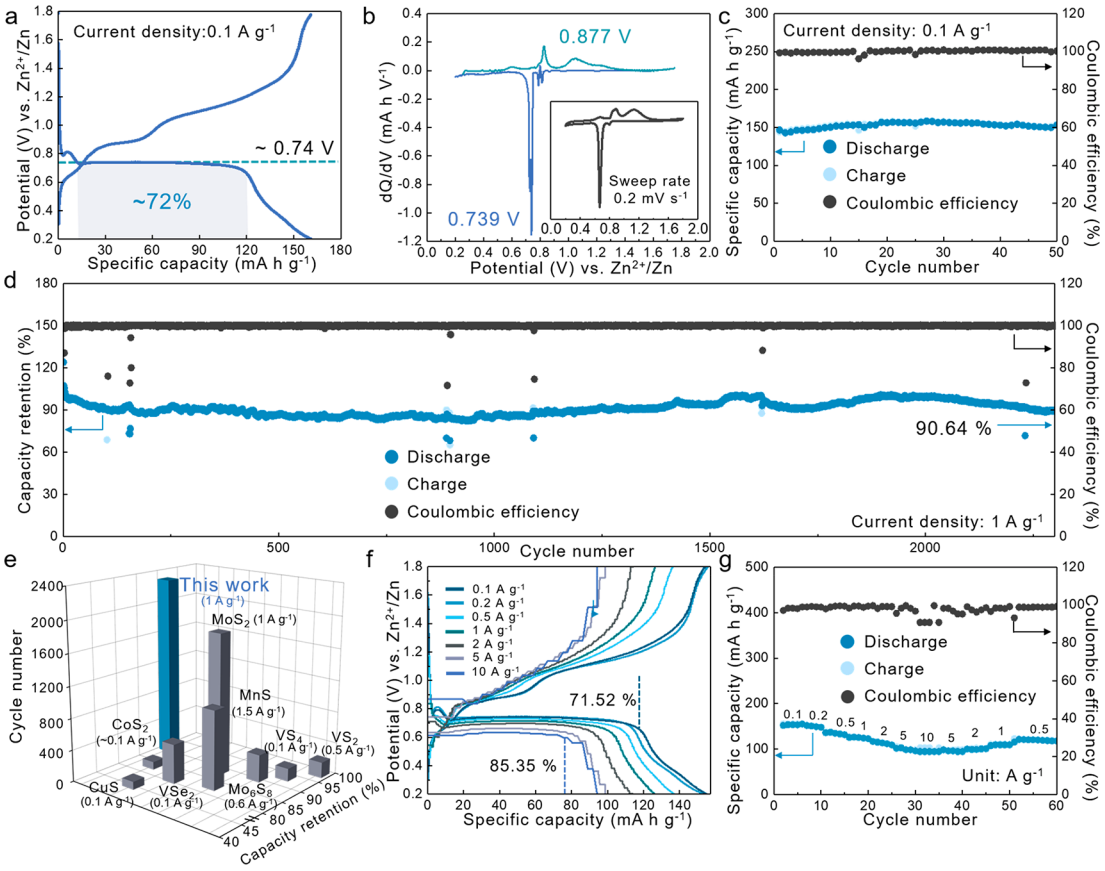

Figure 2. Electrochemical measurement of the BOSN cathode in AZBs. (a) Typical GCD curves and capacity proportion of the discharge plateau at 0.1 A g^{-1}. (b) dQ dV^{-1} of BOSN electrode from GCD curve at 0.1 A g^{-1}, with the inset shown CV curve of the BOSNs at 0.2 mV s^{-1}. (c) Cycling performance at 0.1 A g^{-1}. (d) Long-term stability at 1 A g^{-1}. (e) Contrast of cycling stability between BOSN in this work and TMC-type cathodes in AZBs. (f) Charge/discharge curves at various current densities. (g) Rate cycling performance of the BOSNs.

at −5 °C and works steadily until reaching −15 °C with 81.5% discharge plateau capacity proportion.

RESULTS AND DISCUSSION

The proposed Bi_2O_2Se was grown by the co-melting method from high purity bismuth powder and selenium powder, and ultrathin nanosheets were further obtained by the cryo-mediated liquid-phase exfoliation and fracturing process. The two-dimensional stripped BOSNs exhibit continuous electronic states at the Fermi level and are considered to possess p-type semiconductor properties based on the calculated density of states (Figure 1a, Supporting Information Figure S1). As shown in Figure 1b, the obtained BOSNs display a high degree of crystallization, and all the X-ray diffraction (XRD) patterns can be well indexed to orthorhombic Bi_2O_2Se (JCPDS No. 73-1316) similar to bulk Bi_2O_2Se. The components and morphology of BOSN were characterized by transmission electron microscopy (TEM). As shown in Figure 1c, the single BOSN possesses a nearly transparent uniform appearance, and the lattice distance of ∼0.28 nm in the high-resolution TEM (HRTEM) image (Figure 1d), corresponding to the (110) crystal plane of Bi_2O_2Se, can be clearly indexed. Taking into account the guest-ion insertion/extraction mechanism in the cathode of the electrochemical battery, the ultrathin nanosheet structure (Supporting Information Figure S2) helps provide steady electrochemical performance. The selected area electron diffraction (SAED) pattern was obtained as shown in Figure 1d, further confirming the high crystallinity of the synthesized BOSN and its tetragonal *I4/mmm* space group. Coinciding with the mapping images for bulk Bi_2O_2Se by scanning electron microscopy (SEM) (Supporting Information Figure S3), the TEM images and corresponding elemental mapping images demonstrate the even distribution of Bi, Se, and O in BOSN (Figure 1e–h). Atomic force microscopy (AFM) was performed to estimate the size and thickness of BOSNs (Figure 1i). The BOSNs exhibit a highly uniform size of ∼1 μm with a thickness of either ∼2.5 nm or ∼5 nm, i.e., approximately four or eight layers based on the theoretical thickness of a monolayer ∼0.61 nm (Supporting Information Figure S4), respectively, implying that the shortened ion diffusion distance and the abundance surface sites are conducive to ion insertion and storage.

The structure of the BOSNs was further characterized by using Raman analysis and XPS. The peak centered at 159 cm^{-1} displayed in the Raman spectra (Figure 1j) is identified as A_{1g}, which shows good consistency with prior reports.[27] XPS measurements present the element of Bi, Se, and O in BOSNs, which are inherited from the bulk Bi_2O_2Se (Supporting Information Figure S5). The peaks of the $4f_{5/2}$ and $4f_{7/2}$ core levels of Bi clearly separate at 164.0 and 158.7 eV,[28] respectively, as shown in Supporting Information Figure S6. In addition, the $3d_{3/2}$ and $3d_{5/2}$ peaks of Se appear at 53.4 and 54.3 eV (Supporting Information Figure S7), respectively, which is generally attributed to the uneven distribution and oxidation of selenium on the surface of the nanosheets[29−31] and further causes the O 1s peak to migrate to 529.7 eV

https://doi.org/10.1021/acsnano.1c04636
ACS Nano 2021, 15, 14766−14775

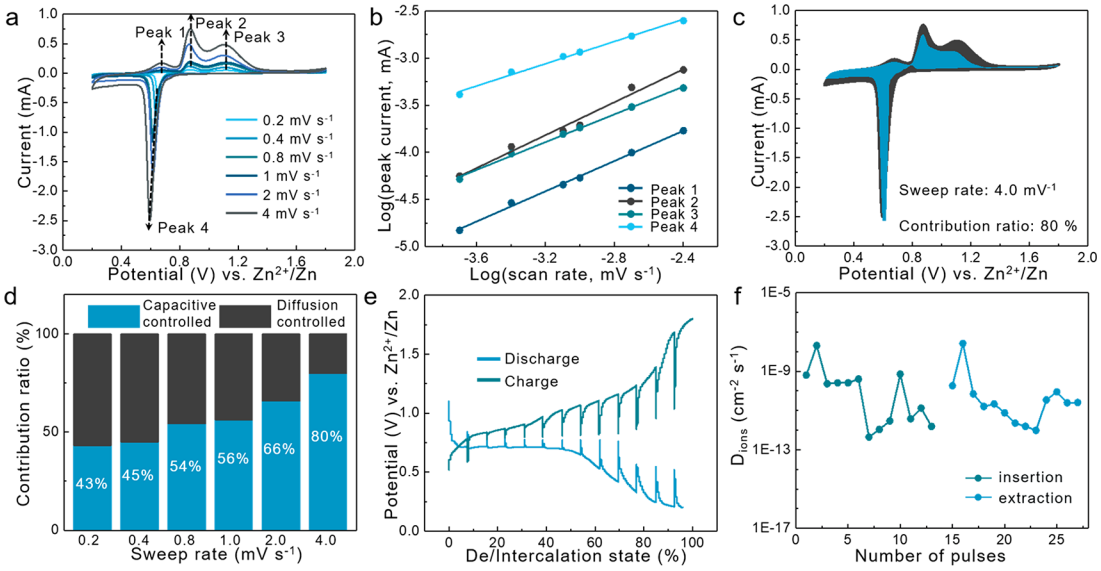

Figure 3. Kinetics analysis for the BOSN cathode. (a) CV curves of the BOSNs under various scan rates. (b) The log(i) versus log(v) curves of the cathodic and anodic peaks of the BOSNs. (c) CV profile at 4.0 mV s^{-1} indicating the capacitive contribution (blue region) to the total current. (d) Contribution ratios of the normalized capacitive (blue) and diffusion-controlled (gray) behavior from 0.2 to 4.0 mV s^{-1}. (e) GITT curves of the BOSNs. (f) Proton diffusion coefficients (D_{ions}) of the BOSN electrode.

(Supporting Information Figure S8). Energy-dispersive X-ray spectroscopy (EDS) provides deeper elemental information because of the desensitization of the surface; the results further confirm the compositional consistency of the BOSNs and bulk Bi_2O_2Se (Figure 1k).

To demonstrate its application in AZBs, full cells were assembled using the as-obtained BOSN as the cathode (Supporting Information Figure S9) and Zn slice as the anode. As depicted in Figure 2a, the galvanostatic charge−discharge (GCD) profiles of the BOSN//Zn battery delivered a capacity of 162 mA h g^{-1} at 0.1 A g^{-1} and further demonstrated stable cycling behavior (Figure 2c), with the Coulombic efficiency (CE) above 99%. It is worth noting that the GCD curves of the BOSNs indicate an ultralong flat plateau near 0.74 V, in which the ultraflat discharge plateau region accounts for 72% of the total capacity (Figure 2a). To further clarify this phenomenon, the corresponding differential capacity versus voltage plot ($dQ\ dV^{-1}$) was calculated. As shown in Figure 2b, a clear sharp decline in voltage hysteresis to 0.739 V is observed, which is believed to be mainly responsible for the high capacity and stable insertion behavior of BOSN, indicating that the high capacity is dominated by redox reaction at the plateaus. The single ultrasharp peak implies the existence of stable two-phase reaction, and the origin of the ultraflat long discharge plateau is also explained. Consistent with the $dQ\ dV^{-1}$ curve, the cyclic voltammetry (CV) curve of the BOSN cathode (Figure 2b) shows a sharp and obvious oxidation peak at ∼0.74 V, which can also be attributed to the insertion process of a single kind of cation in the cathode. In general, most previously reported AZB systems did not possess an obvious discharge plateau or only exhibited a short-curved discharge plateau due to multiphase reaction or solid solution process; thus an ultraflat discharge plateau is considered a long-term pursuit for stable AZB performance, guaranteeing a stable output potential for practical applications.[32] In addition, the morphology of the full-discharged electrode was examined to clarify the types of cations involved in the reaction. Compared with the original black electrode, a large amount of white byproduct was formed on the electrode surface (Supporting Information Figure S10), and the marked lamellar materials, which are usually considered to be zinc sulfate hydroxide hydrate, were observed by SEM (Supporting Information Figure S11). EDS mapping confirms the uniform distribution of elements of Zn, S, and O (Supporting Information Figure S12). Furthermore, dilute sulfuric acid was used to thoroughly remove the surface adhesion layer consisting of zinc sulfate hydroxide hydrate, and a consistent elemental distribution with the original electrode is observed in the corresponding EDS without an observable Zn signal (Supporting Information Figure S13). Therefore, the zinc-ion intercalation chemistry should be excluded, and it can be preliminarily confirmed that the stable two-phase reaction process is proton-dominated (further evidence will be mentioned in the following sections). Stability measurements were performed at 1 A g^{-1}, and a reversible capacity (101 mA h g^{-1}) is obtained (Figure 2d). After more than 2300 cycles, the BOSN//Zn battery indicates a capacity retention (relative to its initial capacity) of 90.64% (Figure 2d), which implies that the BOSN electrode possesses a long-term energy supply capacity. The cycling stability performance of the as-prepared BOSN for AZBs surpasses most previous reported results of transition metal chalcogenides (TMCs)-type cathodes (Figure 2e), such as CuS,[33] VSe_2,[34] CoS_2,[35] MnS,[36] MoS_2,[37] Mo_6S_8,[38] VS_4,[39] and VS_2,[40] suggesting enhanced performance of BOSN for Zn energy storage system and the contribution of proton-dominated electrochemical process to electrode stability.

The rate capacity was also measured as shown in Figure 2g, and the corresponding GCD curves at different rates were shown in Figure 2f. After five cycles for each current density, reversible capacities of 154, 150, 133, 126, 114, 99, and 95 mA h g^{-1} for the BOSN electrode can be achieved at 0.1, 0.2, 0.5, 1, 2, 5 and 10 A g^{-1}, respectively. Notably, even at current densities up to 10 A g^{-1}, the capacity provided by BOSN is only 24.6% less than that provided at 1 A g^{-1}, which possesses excellent merit for abuse tolerance at various current densities. The higher rate capacity relative to the stability measurements

https://doi.org/10.1021/acsnano.1c04636
ACS Nano 2021, 15, 14766−14775

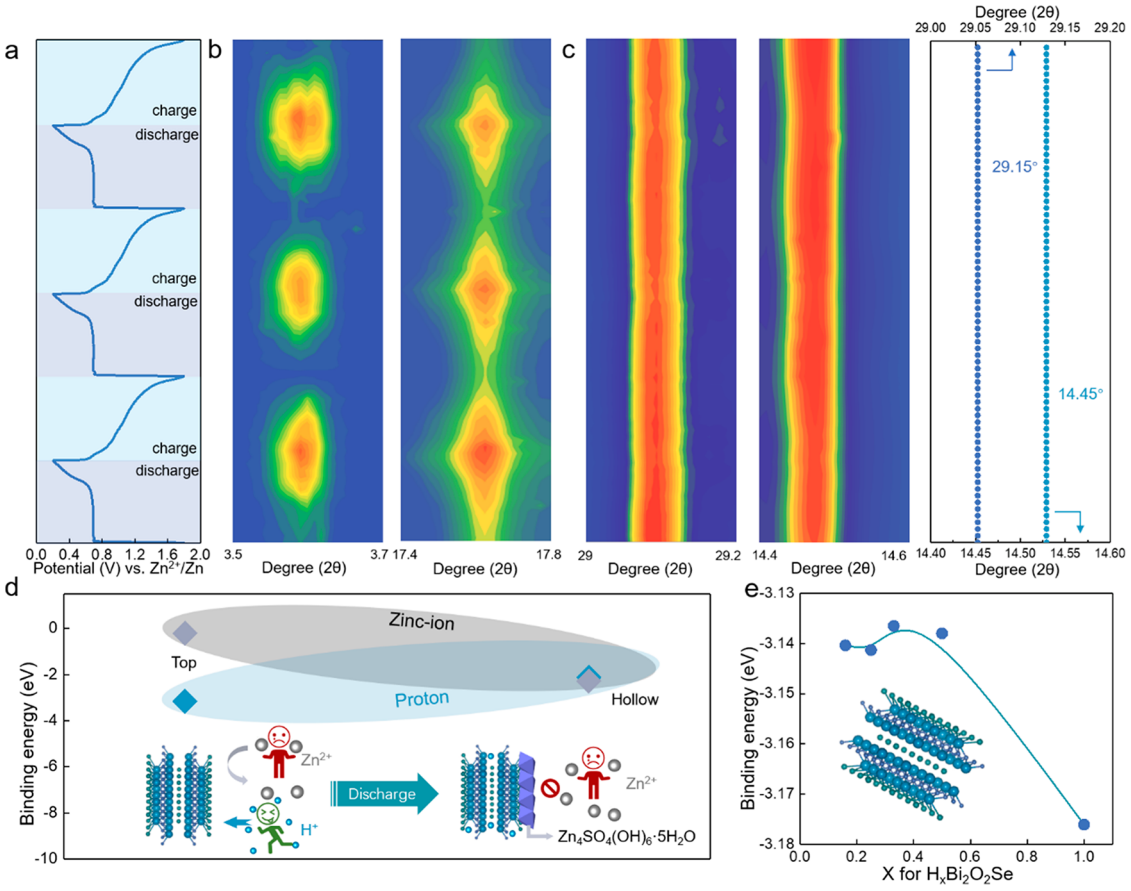

Figure 4. Investigation of the charge storage mechanism for the BOSN electrode. (a) GCD curves during the *in situ* SXRD measurement. (b) Corresponding *in situ* SXRD patterns of the $Zn_4SO_4(OH)_6{\cdot}5H_2O$ byproduct during the GCD scan. (c) Corresponding *in situ* SXRD patterns of the BOSNs during the discharge−charge scan and corresponding peak angle shift curve. (d) Adsorption energy of the original BOSN surface for the protons and Zn ions located in the top and hollow regions, and the illustration shows the ions selectivity of the BOSN electrode during discharge. (e) Variation in the binding energy of the BOSN surface with respect to the number of occupying protons.

may be due to the sufficient activation process. In addition, even the current density increases from 0.1 A g^{-1} to 10 A g^{-1}, and multirate GCD curves still reveal stable and uniform long plateau behaviors. The proportion of platform capacity increases from 71.52% for 0.1 A g^{-1} to 85.35% for 10 A g^{-1} with the weakening of the inclined region caused by the electrical double layer effect, which shows the obviously fast proton-dominated insertion behavior, indicating a consistent electrochemical mechanism (Figure 2f).

To fully illustrate the dynamic process during charge/discharge, CV measurements and galvanostatic intermittent titration technique (GITT) were employed in the BOSN cathode. As revealed by the highly overlapping CV profiles under different scan rates from 0.2 to 4 mV s^{-1} (Figure 3a), the highly reversible de/intercalation process and a stable reaction mechanism in the BOSNs are proved. The relationship between peak currents (i) and scan rates (v) is as follows:

$$i = av^b \tag{1}$$

where a and b are constants. Diffusion-controlled behavior is dominant when the b-value approaches 0.5, and surface-driven behavior is dominant when the b-value is nearly 1.0. The calculated b-values for peaks 1, 2, and 3 are 0.80, 0.87, and 0.74, respectively (Figure 3b), indicating surface-driven behavior, while the electrochemical processes at 0.74 V (peak 4) are diffusion-controlled with a b-value of 0.59. Moreover, the diffusion-controlled behavior contribution can be calculated based on

$$i = k_1v + k_2v^{1/2} \tag{2}$$

where k_1v and $k_2v^{1/2}$ represent the contributions of the diffusion-controlled behavior and surface-driven behavior, respectively. As shown in Figure 3d, as the scan rate increases from 0.2 to 4 mV s^{-1}, the current ratios attributed to the capacitive response increase from 43% at 0.2 mV s^{-1} to a dominant position of 80% at 4 mV s^{-1} (Figure 3c), which can be attributed to the ultrathin nanosheet morphology of BOSN. The kinetics of reaction were further probed via GITT (Figure 3e). It can be observed that D_{ions} decreases slightly and varies from 1.08 × 10^{-12} to 2.29 × 10^{-10} cm^2 s^{-1} and from 7.01 × 10^{-11} to 8.94 × 10^{-11} cm^2 s^{-1} over the total de/intercalation cycle, respectively (Figure 3f). The slow ion diffusion as shown in the Figure 3f can be attributed to the full intercalation of protons, which reflects the typical phase transition behavior.[24] The results suggest that the proton induces a stable one-step phase conversion process of BOSN during the reaction, thus providing a high energy supply at a stable voltage.

Furthermore, *in situ* SXRD is performed to track the phase evolution of the BOSN cathode in the GCD processes between 0.2 and 1.8 V at 0.15 A g^{-1} (Figure 4a). During discharge, new diffraction peaks observed at 3.6° and 17.6° are generated that can be attributed to $Zn_4SO_4(OH)_6{\cdot}5H_2O$ (Figure 4b) and

https://doi.org/10.1021/acsnano.1c04636
ACS Nano 2021, 15, 14766−14775

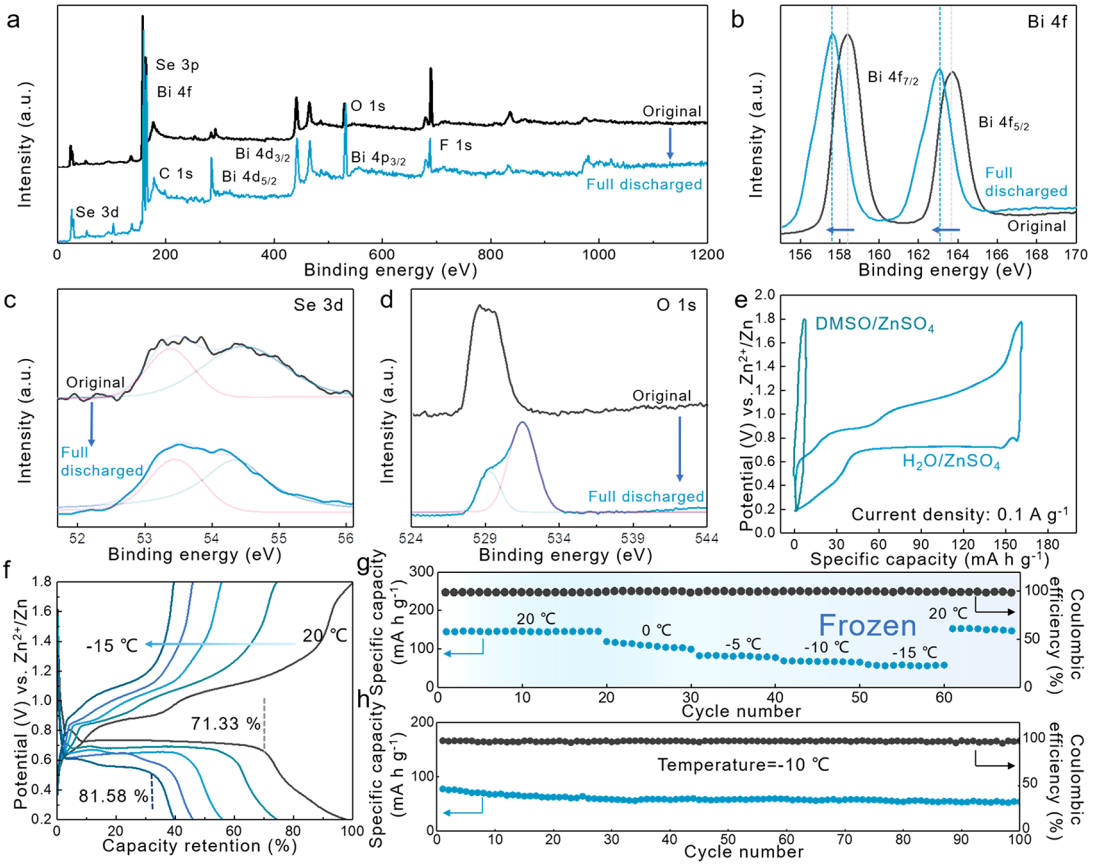

Figure 5. ***Ex situ*** **XPS analysis and low-temperature performance test. (a) Comparison of the XPS spectra before and after discharge. (b) Comparison of the Bi 4f spectra before and after discharge. (c) Comparison of the Se 3d spectra before and after discharge. (d) Comparison of the O 1s spectra before and after discharge. (e) GCD profiles of BOSN in proton-free electrolyte (DMSO) and aqueous solution. (f) GCD curves at 0.1 A g^{-1} and temperatures of 20 °C, 0 °C, −5 °C, −10 °C, and −15 °C. (g) Cycling performance of the BOSN//Zn battery at 0.1 A g^{-1} and temperatures of 20 °C, 0 °C, −5 °C, −10 °C, and −15 °C. (f) Cycling performance at −10 °C with a current density of 0.1 A g^{-1}.**

then gradually disappear after charging. Considering the slightly acidic reaction environment, the reversible formation/decomposition of alkaline $Zn_4SO_4(OH)_6{\cdot}5H_2O$ is generally ascribed to the violent depletion/release of protons by the cathode in the aqueous $ZnSO_4$ electrolyte. During the long flat proton insertion plateau of approximately 0.74 V in the discharge process, massive protons insert into the BOSN cathode stemming from the ionization of H_2O in the electrolyte, which produces additional OH^- and changes the pH of the environment at the cathode interface. Therefore, $Zn_4SO_4(OH)_6{\cdot}5H_2O$ is produced rapidly as a byproduct and stable at the interface due to the alkaline environment. In the following charge process, protons gradually extract from the cathode, and the pH of the environment becomes slightly acidic again, further causing the decomposition of $Zn_4SO_4(OH)_6{\cdot}5H_2O$; notably, the diffraction peak finally disappears at approximately 1.6 V. As mentioned above, the analysis of the peaks assigned to $Zn_4SO_4(OH)_6{\cdot}5H_2O$ clearly illustrate the existence of a process in which a large number of protons participate in the GCD cycles, resulting in the generation of the proton-dominated ultraflat long plateau. Moreover, due to the small radius of a proton, the 29.15° peak and 14.45° peak attributed to the BOSNs show only an invisible oscillation in the whole process (Figure 4e), indicating nearly zero strain of host material during the proton insertion/extraction process. Therefore, the proton-dominated reaction was further confirmed because large zinc ions will lead to an unignorable lattice expansion, and the stable electrode structure for long life span is also guaranteed. By combination of the analysis results above, the reaction on cathode during discharge can be summarized as below:

$$Bi_2O_2Se + 11xH_2O + 4xZn^{2+} + xSO_4^{2-} + 6xe^- \rightarrow H_xBi_2O_2Se + xZn_4SO_4(OH)_6{\cdot}5H_2O$$

In the anode,

$$3xZn - 6xe^- \rightarrow 3xZn^{2+}$$

Correspondingly, the reactions on cathode during charge can be further written as

$$H_xBi_2O_2Se + xZn_4SO_4(OH)_6{\cdot}5H_2O - 6xe^- \rightarrow Bi_2O_2Se + 11xH_2O + 4xZn^{2+} + xSO_4^{2-}$$

And in the anode,

$$3xZn^{2+} + 6xe^- \rightarrow 3xZn$$

DFT calculations were also performed to explain the proton-dominated ion insertion in the BOSNs. According to the proposed storage mechanism, the adsorption energies of the Zn ions and protons on the original BOSN surface were simulated to clarify the occurrence of selective adsorption during cycling. As shown in Figure 4d, the BOSNs show a higher affinity for protons with adsorption energy of −3.15 eV

https://doi.org/10.1021/acsnano.1c04636
ACS Nano 2021, 15, 14766−14775

in the top region and −2.11 eV in the hollow region than for Zn ions with adsorption energy of −0.19 eV in the top region and −2.26 eV in the hollow region, suggesting a tendency for the proton insertion process. The binding energy of the BOSN surface was also calculated for various proportions of occupying protons (Figure 4e). The calculated binding energy of $H_xBi_2O_2Se$ is −3.14 eV for $H_{0.16}Bi_2O_2Se$, −3.141 eV for $H_{0.25}Bi_2O_2Se$, −3.136 eV for $H_{0.33}Bi_2O_2Se$, −3.138 eV for $H_{0.5}Bi_2O_2Se$, and −3.176 eV for HBi_2O_2Se. The adsorption of protons on the BOSN surface thus tends to become saturated, and the low binding energy facilitates the capture and storage of protons, which promotes a large number of protons occupation on the BOSN surface.

As further confirmation of the proposed reaction mechanism, we disassembled the fully discharged BOSN//Zn batteries and characterized the chemical state change of the BOSN electrode. *Ex situ* XPS analysis was used to explore the valence state changes of the elements. Compared with the uncleaned electrode after discharge (Supporting Information Figure S14), there is no obvious signal attributed to Zn and S in the dilute sulfuric acid-cleaned electrode (Figure 5a), consistent with TEM images (Supporting Information Figures S15 and S16). The peaks located at 158.7 and 164.0 eV of Bi 4f move ∼0.9 eV to the low valence state relative to the original BOSN, indicating valid reduction during discharge (Figure 5b). The fine Se 3d spectrum was resolved into two peaks as Se $3d_{5/2}$ and Se $3d_{3/2}$ which were located at 53.4 and 54.3 eV, respectively, and shows that the peak position and ratio have not changed significantly (Figure 5c). In addition, the O 1s signal can be decomposed into 529.7 and 531.5 eV (Figure 5d), and the increased 531.5 eV peak is generally assigned to the bonds of −OH, further indicating the effective insertion of protons.[41] Given that protons play a major role in charge compensation during the electrochemical cycling in BOSN//Zn system with an aqueous 1.0 M $ZnSO_4$ electrolyte, the feasibility of operating needed to be tested in proton-free electrolyte to provide more direct evidence of proton dominance. According to previous reports, the possible proton/Zn-ion co-intercalation can be evaluated by comparing the capacity of electrode in different electrolytes; when dimethyl sulfoxide (DMSO)/$ZnSO_4$ electrolyte is used to provide a proton-free environment, only the Zn ion will be inserted into the cathode.[42] As shown in Figure 5e, GCD profiles are compared to illustrate the role of protons. Impressively, only the BOSN electrode in H_2O/$ZnSO_4$ environment shows mainly ion-interaction stages in discharge curve. As a contrast, BOSN in DMSO/$ZnSO_4$ environment hardly shows effective capacity and lacks the long reaction plateau. The above analysis confirms the insertion of protons rather than Zn ions and is consistent with the *in situ* SXRD analysis.

Considering the stable and fast kinetic behavior of protons in ice,[43] it is necessary to investigate the low-temperature performance of BOSN//Zn batteries. As shown in Figure 5g, the battery shows a specific capacity up to 121, 84, 71, and 65 mA h g^{-1} at low temperatures of 0, −5, −10, and −15 °C, respectively. It is worth noting that the 1 M $ZnSO_4$ electrolyte is frozen at −5 °C; thus, the BOSN//Zn battery successfully operates as a low-temperature solid-state AZB. The corresponding GCD curve is depicted in Figure 5f and shows a similar ultralong plateau, which can still provide 76% discharge plateau capacity proportion even at −5 °C. Owing to the fast dynamics of proton diffusion, the cell operating at −15 °C provides a stable energy supply with 81.58% discharge plate capacity proportion. Moreover, the low-temperature life span test indicates that the proposed cells can still provide 71.4% capacity retention after 100 cycles at −10 °C. Owing to the use of low concentration of electrolyte without additive, the good performance reported here further confirms the enhanced low-temperature coping ability of proton-dominated process.

CONCLUSIONS

In summary, we proposed a high-performance AZB based on the synthesis of Bi_2O_2Se nanosheets and reported a proton-dominated electrochemical insertion/extraction process in AZBs. Benefiting from the ultrasmall size of protons, the BOSN cathode provided a typical capacity of 162 mA h g^{-1} at 0.1 A g^{-1} and further demonstrated a stable cycling capacity of 90.64% capacity retention after 2300 cycles at high rates of 1 A g^{-1}. The GCD curves indicated an ultraflat long proton insertion plateau (72% capacity proportion) at ∼0.74 V, which was consistent with the sharp oxidation peak observed in the CV measurement. Even under icing conditions at −5 °C, the proposed battery also showed a low-temperature performance as 84 mA h g^{-1} and could work steadily until reaching −15 °C with 81.5% plateau capacity proportion. XPS analysis, *in situ* SXRD, and DFT calculations further illustrated the proton insertion mechanism. In view of this proton-dominated process rather than zinc-ion insertion/extraction process in BOSN cathodes, we believe that our work provides a possible method for designing high-performance AZBs and other aqueous batteries.

EXPERIMENTAL SECTION

Materials Synthesis. The Bi_2O_2Se powder was grown by the co-melting method. First, stoichiometric high-purity Bi_2O_3 powder (99.999%), Se powder (99.999%), and Bi powder (99.999%) were weighed and placed into evacuated quartz tubes with pressures down to 10^{-2} Pa. Bi_2O_2Se powder was obtained when the temperature was kept at 773 K for 6 h. Subsequently, the obtained Bi_2O_2Se powder was dispersed in water, placed in a freezer overnight, thawed at room temperature, and sonicated for 30 min. The product was then collected by vacuum filtration. After drying overnight in a 60 °C blast oven, BOSNs were finally obtained and tap density of BOSN is measured as 1660 mg cm^{-3}.

Materials Characterization. The synthesized Bi_2O_2Se samples were characterized by SEM (Carl Zeiss Gemini SEM 300), XPS (Kratos Analytical Axis UltraDLD), TEM (JEM-2100), Raman spectrometer (RENISHAW inVia Basis; 532 nm) and AFM (CSPM-5500).

Electrochemical Evaluation. The Bi_2O_2Se sample was mixed with carbon black and polyvinylidene fluoride in a weight ratio of 7:2:1 in 1-methyl-2-pyrrolidinone, and then the slurry was pasted on carbon paper and dried under vacuum at 60 °C for 12 h. The typical mass loading of active materials is calculated as 1−2 mg cm^{-2}. The CR2025 coin-type cells were assembled using the Bi_2O_2Se and Zn slice as the cathode and anode, a glass fiber membrane as the separator, and 1 M $ZnSO_4$ solution as the electrolyte. The battery used for low-temperature test is assembled the same as the typical Bi_2O_2Se battery at room temperature. The assembled battery is placed in the refrigerator and tested after standing for 2 h at the set temperature to ensure the consistent operation temperature. The GCD test was performed on a LANHE CT2001A battery testing system. The CV test was carried out on a CHI 760E (Chenhua Instrument Company, Shanghai, China) electrochemical workstation.

***In Situ* Synchrotron X-ray Diffraction Experiment.** *In situ* SXRD experiments were performed on the beamline BL02U2 (X-ray wavelength of 0.6887 Å) at Shanghai Synchrotron Radiation Facility (SSRF). The beam size was confined by horizontal and vertical slits to

https://doi.org/10.1021/acsnano.1c04636
ACS Nano 2021, 15, 14766−14775

be approximately 0.3 × 0.3 mm^2. The two-dimensional XRD signal was obtained by a PILATUS3S 2M detector. In addition, a special coin cell was designed for *in situ* SXRD study. There were two observation holes with a radius of ∼2 mm in the middle of two sides of the cell, guaranteeing that X-rays could penetrate through the active material during operation. The special *in situ* cell observation hole is sealed with polyimide tape.

Computational Methods. DFT calculations were carried out with the projector augmented wave (PAW)[44] Vienna *ab Initio* Simulation Package (VASP) code.[45] The generalized gradient approximation (GGA) with the Perdew–Burke–Ernzerhof (PBE) functional[46] was used to describe the electron exchange–correlation potential. The bilayer (BL) Bi_2O_2Se can be regarded as the simplest multilayer Bi_2O_2Se and thus was adapted to calculate the binding energy in this paper for saving time. For the calculations of electronic properties, four layers of unit cell Bi_2O_2Se were used. A 15 Å vacuum layer along the *z*-axis was also inserted to prevent interaction of periodic structures. All atoms were fully relaxed until the maximum force was less than 0.01 eV/Å. The kinetic energy cutoff for the plane-wave basis was set to 400 eV. The k-mesh density based on the Monkhorst–Pack scheme[47] was adapted to less than 0.03 $Å^{-1}$ in the Brillouin zone sampling. The long-range van der Waals interactions at the DFT-D3 level[48] were considered in all calculations.

ASSOCIATED CONTENT

Supporting Information

The Supporting Information is available free of charge at https://pubs.acs.org/doi/10.1021/acsnano.1c04636.

Electrical conductivities, TEM images, AFM images, and XPS spectra of the BOSNs; electrical conductivities, SEM image and the corresponding EDS mapping, and XPS spectrum of the bulk Bi2O2Se; SEM image and the corresponding EDS mapping of the BOSN electrode; optical photograph of the full-discharged BOSN electrode; SEM image and the corresponding EDS mapping of $Zn4SO4(OH)6{\cdot}5H_2O$; EDS spectra of the BOSNs; TEM image and the corresponding EDS mapping, SEM-EDS spectra, and TEM-EDS spectra of full-discharged BOSNs; XPS spectrum of the uncleaned full-discharged BOSN electrode (PDF)

AUTHOR INFORMATION

Corresponding Authors

Xiaolong Li − *Shanghai Institute of Applied Physics, Chinese Academy of Sciences, Shanghai 201800, China; Shanghai Synchrotron Radiation Facility, Shanghai Advanced Research Institute, Chinese Academy of Sciences, Shanghai 201204, China;* orcid.org/0000-0002-1674-9345; Email: lixiaolong@sinap.ac.cn

Renzhong Tai − *Shanghai Institute of Applied Physics, Chinese Academy of Sciences, Shanghai 201800, China; Shanghai Synchrotron Radiation Facility, Shanghai Advanced Research Institute, Chinese Academy of Sciences, Shanghai 201204, China*; Email: tairenzhong@sinap.ac.cn

Daming Zhu − *Shanghai Institute of Applied Physics, Chinese Academy of Sciences, Shanghai 201800, China; Shanghai Synchrotron Radiation Facility, Shanghai Advanced Research Institute, Chinese Academy of Sciences, Shanghai 201204, China;* orcid.org/0000-0003-2094-8360; Email: zhudaming@zjlab.org.cn

Authors

Yuanhe Sun − *Shanghai Institute of Applied Physics, Chinese Academy of Sciences, Shanghai 201800, China; Shanghai Synchrotron Radiation Facility, Shanghai Advanced Research Institute, Chinese Academy of Sciences, Shanghai 201204, China; University of Chinese Academy of Sciences, Beijing 100049, China*

Zhaofeng Lian − *Shanghai Institute of Applied Physics, Chinese Academy of Sciences, Shanghai 201800, China; Shanghai Synchrotron Radiation Facility, Shanghai Advanced Research Institute, Chinese Academy of Sciences, Shanghai 201204, China*

Zhiguo Ren − *Shanghai Institute of Applied Physics, Chinese Academy of Sciences, Shanghai 201800, China; Shanghai Synchrotron Radiation Facility, Shanghai Advanced Research Institute, Chinese Academy of Sciences, Shanghai 201204, China*

Zeying Yao − *Shanghai Institute of Applied Physics, Chinese Academy of Sciences, Shanghai 201800, China; Shanghai Synchrotron Radiation Facility, Shanghai Advanced Research Institute, Chinese Academy of Sciences, Shanghai 201204, China; University of Chinese Academy of Sciences, Beijing 100049, China*

Yaru Yin − *Centre for Transformative Science, ShanghaiTech University, Shanghai 201210, China*

Ping Huai − *Shanghai Institute of Applied Physics, Chinese Academy of Sciences, Shanghai 201800, China; Shanghai Synchrotron Radiation Facility, Shanghai Advanced Research Institute, Chinese Academy of Sciences, Shanghai 201204, China*

Fangyuan Zhu − *Shanghai Institute of Applied Physics, Chinese Academy of Sciences, Shanghai 201800, China; Shanghai Synchrotron Radiation Facility, Shanghai Advanced Research Institute, Chinese Academy of Sciences, Shanghai 201204, China*

Yaobo Huang − *Shanghai Institute of Applied Physics, Chinese Academy of Sciences, Shanghai 201800, China; Shanghai Synchrotron Radiation Facility, Shanghai Advanced Research Institute, Chinese Academy of Sciences, Shanghai 201204, China*

Wen Wen − *Shanghai Institute of Applied Physics, Chinese Academy of Sciences, Shanghai 201800, China; Shanghai Synchrotron Radiation Facility, Shanghai Advanced Research Institute, Chinese Academy of Sciences, Shanghai 201204, China;* orcid.org/0000-0002-5139-9889

Complete contact information is available at: https://pubs.acs.org/10.1021/acsnano.1c04636

Author Contributions

[⊥]Y.S. and Z.L. contributed equally to this work.

Notes

The authors declare no competing financial interest.

ACKNOWLEDGMENTS

This work was financially supported by the National Natural Science Foundation of China (Grants 12005286, U2032204, 11875315, and 52032005), National Key Research and Development Programme of China (Grants 2017YFA0403400 and 2016YFA0401002), the Shanghai Sailing Programme (Grant 19YF1452700), and Natural Science Foundation of Shanghai (Grant 20ZR1464200). The authors thank the staffs from beamlines 02U2, 14B1, 17B1, 15U1 and Materials Assistant Laboratory at SSRF for technical support.

REFERENCES

(1) Ma, L.; Chen, S.; Long, C.; Li, X.; Zhao, Y.; Liu, Z.; Huang, Z.; Dong, B.; Zapien, J. A.; Zhi, C. Achieving High-Voltage and High-Capacity Aqueous Rechargeable Zinc Ion Battery by Incorporating Two-Species Redox Reaction. *Adv. Energy Mater.* **2019**, *9*, 1902446.

(2) Zhang, N.; Cheng, F.; Liu, J.; Wang, L.; Long, X.; Liu, X.; Li, F.; Chen, J. Rechargeable Aqueous Zinc-Manganese Dioxide Batteries with High Energy and Power Densities. *Nat. Commun.* **2017**, *8*, 405.

(3) Wan, F.; Zhang, L.; Dai, X.; Wang, X.; Niu, Z.; Chen, J. Aqueous Rechargeable Zinc/Sodium Vanadate Batteries with Enhanced Performance from Simultaneous Insertion of Dual Carriers. *Nat. Commun.* **2018**, *9*, 1656.

(4) Huang, J.; Wang, Z.; Hou, M.; Dong, X.; Liu, Y.; Wang, Y.; Xia, Y. Polyaniline-Intercalated Manganese Dioxide Nanolayers as a High-Performance Cathode Material for an Aqueous Zinc-Ion Battery. *Nat. Commun.* **2018**, *9*, 2906.

(5) Liu, H.; Zhu, Z.; Yan, Q.; Yu, S.; He, X.; Chen, Y.; Zhang, R.; Ma, L.; Liu, T.; Li, M.; Lin, R.; Chen, Y.; Li, Y.; Xing, X.; Choi, Y.; Gao, L.; Cho, H. S.-y.; An, K.; Feng, J.; Kostecki, R.; Ami.; et al. A Disordered Rock Salt Anode for Fast-Charging Lithium-Ion Batteries. *Nature* **2020**, *585*, 63−67.

(6) Ren, X. C.; Zhao, Y. X.; Li, Q. W.; Cheng, F.; Wen, W.; Zhang, L. L.; Huang, Y. B.; Xia, X. H.; Li, X. L.; Zhu, D. M.; Huo, K. F.; Tai, R. Z. A Novel Multielement Nanocomposite with Ultrahigh Rate Capacity and Durable Performance for Sodium-Ion Battery Anodes. *J. Mater. Chem. A* **2020**, *8*, 11598−11606.

(7) Yang, Q.; Mo, F.; Liu, Z.; Ma, L.; Li, X.; Fang, D.; Chen, S.; Zhang, S.; Zhi, C. Activating C-Coordinated Iron of Iron Hexacyanoferrate for Zn Hybrid-Ion Batteries with 10 000-Cycle Lifespan and Superior Rate Capability. *Adv. Mater.* **2019**, *31*, 1901521.

(8) Chao, D.; Zhu, C.; Song, M.; Liang, P.; Zhang, X.; Tiep, N. H.; Zhao, H.; Wang, J.; Wang, R.; Zhang, H.; Fan, H. J. A High-Rate and Stable Quasi-Solid-State Zinc-Ion Battery with Novel 2D Layered Zinc Orthovanadate Array. *Adv. Mater.* **2018**, *30*, 1803181.

(9) Ni, Q.; Jiang, H.; Sandstrom, S.; Bai, Y.; Ren, H.; Wu, X.; Guo, Q.; Yu, D.; Wu, C.; Ji, X. A $Na_3V_2(PO_4)_2O_{1.6}F_{1.4}$ Cathode of Zn-Ion Battery Enabled by a Water-in-Bisalt Electrolyte. *Adv. Funct. Mater.* **2020**, *30*, 2003511.

(10) Li, X.; Li, M.; Yang, Q.; Wang, D.; Ma, L.; Liang, G.; Huang, Z.; Dong, B.; Huang, Q.; Zhi, C. Vertically Aligned Sn^{4+} Preintercalated Ti_2CTX MXene Sphere with Enhanced Zn Ion Transportation and Superior Cycle Lifespan. *Adv. Energy Mater.* **2020**, *10*, 2001394.

(11) Liang, H.; Cao, Z.; Ming, F.; Zhang, W.; Anjum, D. H.; Cui, Y.; Cavallo, L.; Alshareef, H. N. Aqueous Zinc-Ion Storage in MoS_2 by Tuning the Intercalation Energy. *Nano Lett.* **2019**, *19*, 3199−3206.

(12) Liu, J.; Xu, P.; Liang, J.; Liu, H.; Peng, W.; Li, Y.; Zhang, F.; Fan, X. Boosting Aqueous Zinc-Ion Storage in MoS_2 *via* Controllable Phase. *Chem. Eng. J.* **2020**, *389*, 124405.

(13) Owusu, K. A.; Pan, X.; Yu, R.; Qu, L.; Liu, Z.; Wang, Z.; Tahir, M.; Haider, W. A.; Zhou, L.; Mai, L. Introducing Na_2SO_4 in Aqueous $ZnSO_4$ Electrolyte Realizes Superior Electrochemical Performance in Zinc-Ion Hybrid Capacitor. *Mater. Today Energy* **2020**, *18*, 100529.

(14) Hu, P.; Zhu, T.; Wang, X.; Zhou, X.; Wei, X.; Yao, X.; Luo, W.; Shi, C.; Owusu, K. A.; Zhou, L.; Mai, L. Aqueous Zn//$Zn(CF_3SO_3)_2$//$Na_3V_2(PO_4)_3$ Batteries with Simultaneous Zn^{2+}/Na^+ Intercalation/De-Intercalation. *Nano Energy* **2019**, *58*, 492−498.

(15) Huang, J.; Wang, Z.; Hou, M.; Dong, X.; Liu, Y.; Wang, Y.; Xia, Y. Polyaniline-Intercalated Manganese Dioxide Nanolayers as a High-Performance Cathode Material for an Aqueous Zinc-Ion Battery. *Nat. Commun.* **2018**, *9*, 2906.

(16) Wan, F.; Zhang, L.; Dai, X.; Wang, X.; Niu, Z.; Chen, J. Aqueous Rechargeable Zinc/Sodium Vanadate Batteries with Enhanced Performance from Simultaneous Insertion of Dual Carriers. *Nat. Commun.* **2018**, *9*, 1656.

(17) Li, L. P.; Liu, S. L.; Liu, W. C.; Ba, D. L.; Liu, W. Y.; Gui, Q. Y.; Chen, Y.; Hu, Z. Q.; Li, Y. Y.; Liu, J. P. Electrolyte Concentration Regulation Boosting Zinc Storage Stability of High-Capacity $K_{0.486}V_2O_5$ Cathode for Bendable Quasi-Solid-State Zinc Ion Batteries. *Nano-Micro Lett.* **2021**, *13*, 34.

(18) Grinin, A.; Matveev, A.; Yost, D. C.; Maisenbacher, L.; Wirthl, V.; Pohl, R.; Hansch, T. W.; Udem, T. Two-Photon Frequency Comb Spectroscopy of Atomic Hydrogen. *Science* **2020**, *370*, 1061−1066.

(19) Wu, X.; Hong, J. J.; Shin, W.; Ma, L.; Liu, T.; Bi, X.; Yuan, Y.; Qi, Y.; Surta, T. W.; Huang, W.; Neuefeind, J.; Wu, T.; Greaney, P. A.; Lu, J.; Ji, X. Diffusion-Free Grotthuss Topochemistry for High-Rate and Long-Life Proton Batteries. *Nat. Energy* **2019**, *4*, 123−130.

(20) Strietzel, C.; Sterby, M.; Huang, H.; Stromme, M.; Emanuelsson, R.; Sjodin, M. An Aqueous Conducting Redox-Polymer-Based Proton Battery That Can Withstand Rapid Constant-Voltage Charging and Sub-Zero Temperatures. *Angew. Chem., Int. Ed.* **2020**, *59*, 9631−9638.

(21) Wang, L.; Huang, K.-W.; Chen, J.; Zheng, J. Ultralong Cycle Stability of Aqueous Zinc-Ion Batteries with Zinc Vanadium Oxide Cathodes. *Sci. Adv.* **2019**, *5*, No. eaax4279.

(22) Zhao, Q.; Song, A.; Zhao, W.; Qin, R.; Ding, S.; Chen, X.; Song, Y.; Yang, L.; Lin, H.; Li, S.; Pan, F. Boosting the Energy Density of Aqueous Batteries *via* Facile Grotthuss Proton Transport. *Angew. Chem., Int. Ed.* **2021**, *60*, 4169−4174.

(23) Zhang, H.; Wu, W.; Liu, Q.; Yang, F.; Shi, X.; Liu, X.; Yu, M.; Lu, X. Interlayer Engineering of α-MoO_3 Modulates Selective Hydronium Intercalation in Neutral Aqueous Electrolyte. *Angew. Chem., Int. Ed.* **2021**, *60*, 896−903.

(24) Liang, G.; Mo, F.; Wang, D.; Li, X.; Huang, Z.; Li, H.; Zhi, C. Commencing Mild Ag−Zn Batteries with Long-Term Stability and Ultra-Flat Voltage Platform. *Energy Stor. Mater.* **2020**, *25*, 86−92.

(25) Wang, D. H.; Zhao, Y. W.; Liang, G. J.; Mo, F. N.; Li, H. F.; Huang, Z. D.; Li, X. L.; Tang, T. C.; Dong, B. B.; Zhi, C. Y. A Zinc Battery with Ultra-Flat Discharge Plateau through Phase Transition Mechanism. *Nano Energy* **2020**, *71*, 104583.

(26) Peng, L.; Ren, X. C.; Liang, Z. F.; Sun, Y. H.; Zhao, Y. X.; Zhang, J. Q.; Yao, Z. Y.; Ren, Z. G.; Li, Z.; Wang, J.; Zhu, B. E.; Gao, Y.; Wen, W.; Huang, Y. B.; Li, X. L.; Tai, R. Z.; Yang, K.; Zhu, D. M. Reversible Proton Co-Intercalation Boosting Zinc-Ion Adsorption and Migration Abilities in Bismuth Selenide Nanoplates for Advanced Aqueous Batteries. *Energy Stor. Mater.* **2021**, *42*, 34−41.

(27) Fu, Q.; Zhu, C.; Zhao, X.; Wang, X.; Chaturvedi, A.; Zhu, C.; Wang, X.; Zeng, Q.; Zhou, J.; Liu, F.; Tay, B. K.; Zhang, H.; Pennycook, S. J.; Liu, Z. Ultrasensitive 2D Bi_2O_2Se Phototransistors on Silicon Substrates. *Adv. Mater.* **2019**, *31*, 1804945.

(28) Sun, Y.; Ye, S.; Zhang, J.; Song, J.; Zhou, F.; Qu, J. Lithium Nitrate-Assisted Hydrothermal Synthesis of Ultrathin Bi_2O_2Se Nanosheets and Their Photoelectrochemical Performance. *J. Mater. Chem. C* **2020**, *8*, 14711−14717.

(29) Ghosh, T.; Samanta, M.; Vasdev, A.; Dolui, K.; Ghatak, J.; Das, T.; Sheet, G.; Biswas, K. Ultrathin Free-Standing Nanosheets of Bi_2O_2Se: Room Temperature Ferroelectricity in Self-Assembled Charged Layered Heterostructure. *Nano Lett.* **2019**, *19*, 5703−5709.

(30) Chen, C.; Wang, M.; Wu, J.; Fu, H.; Yang, H.; Tian, Z.; Tu, T.; Peng, H.; Sun, Y.; Xu, X.; Jiang, J.; Schröter, N. B. M.; Li, Y.; Pei, D.; Liu, S.; Ekahana, S. A.; Yuan, H.; Xue, J.; Li, G.; Jia, J.; et al. Electronic Structures and Unusually Robust Bandgap in an Ultrahigh-Mobility Layered Oxide Semiconductor, Bi_2O_2Se. *Sci. Adv.* **2018**, *4*, No. eaat8355.

(31) Ding, D.; Jiang, Z.; Ji, D.; Nosang Vincent, M.; Zan, L. Bi_2O_2Se as a Novel Co-Catalyst for Photocatalytic Hydrogen Evolution Reaction. *Chem. Eng. J.* **2020**, *400*, 125931.

(32) Chen, Z.; Yang, Q.; Mo, F.; Li, N.; Liang, G.; Li, X.; Huang, Z.; Wang, D.; Huang, W.; Fan, J.; Zhi, C. Aqueous Zinc−Tellurium Batteries with Ultraflat Discharge Plateau and High Volumetric Capacity. *Adv. Mater.* **2020**, *32*, 2001469.

(33) Ren, W.; Xiong, F.; Fan, Y.; Xiong, Y.; Jian, Z. Hierarchical Copper Sulfide Porous Nanocages for Rechargeable Multivalent-Ion Batteries. *ACS Appl. Mater. Interfaces* **2020**, *12*, 10471−10478.

(34) Wu, Z.; Lu, C.; Wang, Y.; Zhang, L.; Jiang, L.; Tian, W.; Cai, C.; Gu, Q.; Sun, Z.; Hu, L. Ultrathin VSe_2 Nanosheets with Fast Ion

https://doi.org/10.1021/acsnano.1c04636
ACS Nano 2021, 15, 14766−14775

Diffusion and Robust Structural Stability for Rechargeable Zinc-Ion Battery Cathode. *Small* **2020**, *16*, 2000698.
(35) Zhang, R.; Pan, C.; Nuzzo, R. G.; Gewirth, A. A. CoS2 as a Sulfur Redox-Active Cathode Material for High-Capacity Non-aqueous Zn Batteries. *J. Phys. Chem. C* **2019**, *123*, 8740−8745.
(36) Chen, X.; Li, W.; Xu, Y.; Zeng, Z.; Tian, H.; Velayutham, M.; Shi, W.; Li, W.; Wang, C.; Reed, D.; Khramtsov, V. V.; Li, X.; Liu, X. Charging Activation and Desulfurization of MnS Unlock the Active Sites and Electrochemical Reactivity for Zn-Ion Batteries. *Nano Energy* **2020**, *75*, 104869.
(37) Li, S.; Liu, Y.; Zhao, X.; Shen, Q.; Zhao, W.; Tan, Q.; Zhang, N.; Li, P.; Jiao, L.; Qu, X. Sandwich-Like Heterostructures of MoS_2/Graphene with Enlarged Interlayer Spacing and Enhanced Hydrophilicity as High-Performance Cathodes for Aqueous Zinc-Ion Batteries. *Adv. Mater.* **2021**, *33*, 2007480.
(38) Mei, L.; Xu, J.; Wei, Z.; Liu, H.; Li, Y.; Ma, J.; Dou, S. Chevrel Phase Mo_6T_8 (T = S, Se) as Electrodes for Advanced Energy Storage. *Small* **2017**, *13*, 1701441.
(39) Qin, H.; Yang, Z.; Chen, L.; Chen, X.; Wang, L. A High-Rate Aqueous Rechargeable Zinc Ion Battery Based on The VS_4@rGO Nanocomposite. *J. Mater. Chem. A* **2018**, *6*, 23757−23765.
(40) He, P.; Yan, M.; Zhang, G.; Sun, R.; Chen, L.; An, Q.; Mai, L. Layered VS_2 Nanosheet-Based Aqueous Zn Ion Battery Cathode. *Adv. Energy Mater.* **2017**, *7*, 1601920.
(41) Kan, J.; Wang, H.; Zhang, H.; Shi, J.; Liu, W.; Li, D.; Dong, G.; Yang, Y.; Gao, R. Nitrogen Functionalized Carbon Nanocages Optimized as High-Performance Anodes for Sodium Ion Storage. *Electrochim. Acta* **2019**, *304*, 192−201.
(42) Zhao, Q.; Song, A.; Zhao, W.; Qin, R.; Ding, S.; Chen, X.; Song, Y.; Yang, L.; Lin, H.; Li, S.; Pan, F. Boosting the Energy Density of Aqueous Batteries *via* Facile Grotthuss Proton Transport. *Angew. Chem., Int. Ed.* **2021**, *60*, 4169−4174.
(43) Yan, L.; Huang, J.; Guo, Z.; Dong, X.; Wang, Z.; Wang, Y. Solid-State Proton Battery Operated at Ultralow Temperature. *ACS Energy Lett.* **2020**, *5*, 685−691.
(44) Blochl, P. E. Projector Augmented-Wave Method. *Phys. Rev. B: Condens. Matter Mater. Phys.* **1994**, *50*, 17953−17979.
(45) Kresse, G.; Furthmuller, J. Efficient Iterative Schemes for *ab Initio* Total-Energy Calculations Using a Plane-Wave Basis Set. *Phys. Rev. B: Condens. Matter Mater. Phys.* **1996**, *54*, 11169−11186.
(46) Perdew, J. P.; Burke, K.; Ernzerhof, M. Generalized Gradient Approximation Made Simple. *Phys. Rev. Lett.* **1996**, *77*, 3865−3868.
(47) Monkhorst, H. J.; Pack, J. D. Special Points for Brillouin-Zone Integrations. *Phys. Rev. B* **1976**, *13*, 5188.
(48) Grimme, S.; Antony, J.; Ehrlich, S.; Krieg, H. A Consistent and Accurate *ab Initio* Parametrization of Density Functional Dispersion Correction (DFT−D) for the 94 Elements H−Pu. *J. Chem. Phys.* **2010**, *132*, 154104.

https://doi.org/10.1021/acsnano.1c04636
ACS Nano 2021, 15, 14766−14775